STEADY AND UNSTEADY CALCULATIONS ON FULL CONFIGURATION OF TWO-STAGE SPACE TRANSPORTATION SYSTEM DURING SEPARATION

Mochammad Agoes Moelyadi, Christian Breitsamter, Boris Laschka
Institute for Fluid Mechanics, Aerodynamics Divison, Technische Universität München,
Boltzmannstr. 15, D-85747 Garching, Germany

Keywords: *unsteady aerodynamics, TSTO space transportation system, computational fluid dynamics*

Abstract

Steady and Unsteady Euler calculations are carried out to simulate the flow physical phenomena of two stage transportation system during a separation manoeuvre. The computational results of both orbital and carrier stages will be compared to experimental results for several altitudes at separating condition of Mach number 4.0. From the experimental investigation, the complex interactions of incident and reflected shock waves and expansion waves with each other occur in the flow region between the orbital and carrier stages. The changes of distance and incidence between the two stages during the separation process affect the position and intensity of the shockwaves, also the points of interaction of the reflected shockwaves change. This shock interactions cause strong unsteady airloads on both stages.

The simulations are based on a finite volume shock capturing method for solution of the integral form of 3-D unsteady Euler equations. The numerical fluxes are evaluated by the modified AUSM method. The MUSCLE approach is used to obtain the high order accuracy of the left and right states at the cell surface. Furthermore, the initial structured multiblock grid are generated using ICEMCFD. The change of meshes on the flow domain for unsteady calculation is performed by applying a concept of dynamic grid based on solution of Poisson equation. The results include Mach number and density flow contours as well as the aerodynamic coefficients of the orbital and carrier stages.

1 Introduction

To send satellites, machines, etc., even people to orbit as cheaply as possible, next generation space transportation systems are developed to pursue the goal of significantly reducing the costs for space transportation. For this economical purpose the Reusable Launch Vehicles (RLV) have been researched in many hypersonic technological areas in many institutions all over the world [1], such as in the United Stated with NASP (National Aerospace Plane), in Japan with the Aerospace plane of the National Aerospace Laboratory, and in Great Britain with HOTOL (Horizontal Take-Off and Landing).

In Europe some national programs favour to investigate Two-Stage-To-Orbit (TSTO) systems instead of Single-Stage-To-Orbit (SSTO) vehicles. The advanced concepts of TSTO space vehicles are to provide a first stage belonging to a new generation of hypersonic aircrafts with conventional take-off and landing capabilities equipped with airbreathing propulsion. These concepts have been developed in Germany within the ASTRA program and in French within the STAR-H program.

Efforts to develop such hypersonic transportation systems until this time have been performed in Europe with substantial advancements in lightweight, high temperature structural materials, thermal protection systems, propulsion system, etc. Particularly, intensive efforts dealing with the key technologies for a

two-stage space transportation system have been made at Technische Universität München. The designed concept of a fully two-stage hypersonic vehicle deals with a delta-winged first stage powered by airbreathing engines [2], Fig. 1.

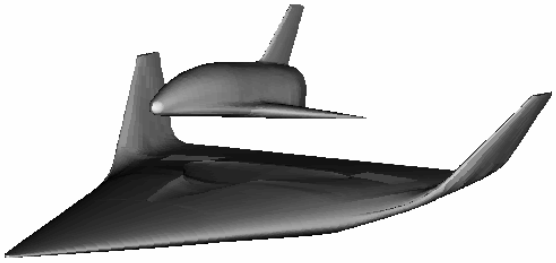

Fig.1. The Fully Two-Stage Space Vehicle.

It is launched horizontally with the orbital stage mounted on the back-top of the hypersonic aircraft to reach the speed flight of approximately Mach 6.8 at altitude of 35 km. On this position the orbital stage is released and the "Separation process" starts. Then, the upper stage continues the ascent to the orbit while the lower stage flies back to its launch site like an aircraft [3].

The separation manoeuvre will be one of the critical phases of the ascent flight mission for the vehicle system. In such a phase, very high dynamic pressures are subject to the space vehicle system. Under these conditions the aerodynamic interferences between the stages may have an impact on the stability of the vehicle during the separation manoeuver, and may cause a great failure during the space vehicle operation.

The problems related to separation manoeuvre have been investigated in numerous experimental and numerical studies. In 1960s, Decker and Gera have performed analysis of the aerodynamic performance of space transportation models for Mach number 3 and 6 during separation [4], where the aerodynamic data obtained constitutes the input for the system of equations of dynamic motion. Then, during the Space Shuttle program, several measurements and calculations dealing with the separation of the liquid-fuel tank from the shuttle orbiter were accomplished [5]. Experimental studies [6, 7] deal with separation of two winged stages. These results extend the knowledge on this class of complicated flows and are necessary for testing the numerical method developed. The results of numerical simulation of the flow around an aerospace system in the course of separation of the stages are described in [8]. However, all investigations assume a steady flowfield and, thus, neglect additional velocities induced from the separation maneuver. Based on the results of Euler solutions Rochholz et al. showed that the effects of unsteady flows during separation due to the shock interactions between the upper stage and lower stage are non-negligible [9]. This indication is also supported by Cvrlje et al. who performed numerical simulation involving both roll and yaw oscillations of an orbital vehicle for different reduced frequencies [10]. Although, the phenomena of unsteady flows on two stage space vehicles have a significant effect on safety during separation maneuver less investigations exist for unsteady cases as presented in Refs. 11, 12, and 13. Especially the problem of unsteady flows for the complex two-stage space vehicle is of major concern.

This paper presents numerical simulations of the physical flow phenomena during the separation manoeuvre of the two-stage transportation system. The computational procedure of the solution of the unsteady Euler equations used to obtain the hypersonic flow simulation around the complex geometry of the two-stage space vehicle will be explained. The computational results of both orbital and carrier stages will be compared to the corresponding experimental data for several altitudes at separating condition. In addition, the influences of "separation" parameters such as the relative angle of attack and relative distance on the flow behavior and aerodynamic characteristics of the space vehicle will be analyzed. Finally, the simulation of real flow condition during the separation process including effects of a downwash corresponding to the orbital motion will be investigated in detail.

2 Numerical Method

2.1 Euler Equations

In the present analysis, the unsteady hypersonic flow around the space vehicle is modeled as three-dimensional, inviscid compressible and adiabatic. For these conditions, the governing flow equations are the three-dimensional Euler equations and may be expressed in strong conservation form and curvilinear coordinates for moving grids as [14]

$$\frac{\partial Q}{\partial \tau}+\frac{\partial F}{\partial \xi}+\frac{\partial G}{\partial \eta}+\frac{\partial H}{\partial \zeta}=\mathbf{0} \qquad (1)$$

Where $\boldsymbol{Q}$ is the vector of conservative variables times the Jacobian transformation, $\boldsymbol{J}$. While, $\boldsymbol{F}$, $\boldsymbol{G}$, and $\boldsymbol{H}$ are the conservative fluxes with respect to the ξ, η, and ζ directions:

$$Q=J\begin{bmatrix}\rho\\ \rho u\\ \rho v\\ \rho w\\ e\end{bmatrix},\quad F=J\begin{bmatrix}\rho U\\ \rho uU+\xi_x p\\ \rho vU+\xi_y p\\ \rho wU+\xi_z p\\ U(e+p)-\xi_t p\end{bmatrix}$$

$$G=J\begin{bmatrix}\rho V\\ \rho uV+\eta_x p\\ \rho vV+\eta_y p\\ \rho wV+\eta_z p\\ V(e+p)-\eta_t p\end{bmatrix}\quad H=J\begin{bmatrix}\rho W\\ \rho uW+\varsigma_x p\\ \rho vW+\varsigma_y p\\ \rho wW+\varsigma_z p\\ W(e+p)-\varsigma_t p\end{bmatrix}$$

With the contravariant velocities

$$\begin{aligned}U&=\xi_x u+\xi_y v+\xi_z w+\xi_t\\ V&=\eta_x u+\eta_y v+\eta_z w+\eta_t\\ W&=\varsigma_x u+\varsigma_y v+\varsigma_z w+\varsigma_t\end{aligned} \qquad (2)$$

As closure condition based on the assumption of perfect gas, the following state equation is necessary.

$$p=(\gamma-1)\left[e-\tfrac{1}{2}\rho\left(u^2+v^2+w^2\right)\right] \qquad (3)$$

where $\gamma=c_p/c_v$. More details concerning the metric terms and Jacobian transformation and the used numerical solver can be found in [9, 10, 11, 14].

2.2 Numerical Procedure

The calculation of the vector of conservative variables $\boldsymbol{Q}$ is performed by means of a finite volume approximation to Eq. (1) using an explicit time integration. Based on this approximation, the conservation variables are constant in an infinite small volume element. Corresponding to different time, state variables will be changed by the flux flow through the face of the small cell. Associating grid indexes l, m, and n with the ξ, η, and ζ directions, the numerical approximation may be expressed in a discrete conservation law form given by

$$\begin{aligned}\frac{\partial Q_{l,m,n}}{\partial \tau}=&-\left(F_{l+\frac{1}{2},m,n}-F_{l-\frac{1}{2},m,n}\right)/(\Delta\xi)\\ &-\left(G_{l,m+\frac{1}{2},n}-G_{l,m-\frac{1}{2},n}\right)/(\Delta\eta)\\ &-\left(H_{l,m,n+\frac{1}{2}}-H_{l,m,n-\frac{1}{2}}\right)/(\Delta\varsigma)\end{aligned} \qquad (4)$$

The evaluation of the numerical fluxes between cells is performed by the modified AUSM ('Advection Upstream Splitting Method') according to Radespiel et. al. [15]. This scheme represents a hybrid approach between the van Leer flux vector splitting scheme and the original AUSM scheme developed by Liou and Steffen [16]. The AUSM scheme is based on the idea to regard the convection and acoustic waves as physically distinct processes and thus define the fluxes as a sum of the convective and pressure terms. Applying the modified AUSM scheme, the discretization of the flux vector including mass, momentum and energy in the ξ direction at a cell surface ($l+1/2, m, n$), which is the middle surface between cell (l, m, n) and cell ($l+1,m, n$), can be written as:

$$F_{l+\frac{1}{2},m,n}=F^{c}_{l+\frac{1}{2},m,n}+P_{l+\frac{1}{2},m,n} \qquad (5)$$

The $F^{c}_{l+\frac{1}{2},m,n}$ is characterized with a advective Mach number and a scalar dissipative term.

$$F^{c}_{l+\frac{1}{2},m,n} = \left\{ \frac{1}{2} \mathrm{M}_{l+1/2,m,n} \left(W_{l+1,m,n} + W_{l,m,n} \right) \right. \\ \left. - \frac{1}{2} \Phi_{l+1/2,m,n} \left(W_{l+1,m,n} - W_{l,m,n} \right) \right\} |S|_{l+1/2,m,n} \quad (6)$$

Where $W = (\rho c, \rho uc, \rho vc, \rho wc, \rho Hc)^T$ and the surface vector $S_{l+\frac{1}{2},m,n} = (s_x, s_y, s_z)^T_{l+\frac{1}{2},m,n}$ which its components are normal to the ξ, η, and ζ directions, respectively. Furthermore, the total enthapy $H = (e + p)/\rho$, and c is the speed of sound.

The pressure term in eq. (5) can be written as:

$$P_{l+1/2,m,n} = p_{l+1/2,m,n} (0, s_x, s_y, s_z, 0)^T \quad (7)$$

Both the advective Mach number and the pressure term are determined from the wave velocity $M^{\pm}$ and pressure $p^{\pm}$ on the cell (m,l,n) and $(l+1,m,n)$, respectively.

Radespiel et. al. introduce the dissipative term, $\Phi_{l+1/2,m,n}$ in eq. (6) as a combination of numerical dissipation in the AUSM scheme and the Flux Vector Splitting method.

$$\Phi_{l+1/2,m,n} = (1-\omega)\Phi^{VL}_{l+1/2,m,n} + \omega \Phi^{\mathrm{mod}\,AUSM}_{l+1/2,m,n} \quad (8)$$

The definitions of the dissipation of the Flux Vector Splitting method $\Phi^{VL}_{l+1/2,m,n}$ and of the AUSM $\Phi^{\mathrm{mod}\,AUSM}_{l+1/2,m,n}$, as well as the dissipative parameter ω are explained for example in [14].

The order of approximation in space depends on the value of right and left state variables. To guarantee high order accuracy in the spatial domain, the left and right states at the cell surface are obtained with the MUSCL (Monotonic Upstream Scheme for Conservation Laws) extrapolation method. The limiter function such as a van Albada limiter can be chosen to extrapolate the state values and thus provide high-order fluxes in smooth regions. At discontinuties the limiter function switches to first-order accuracy to ensure optimal shock-capturing features.

On impermeable wall characteristic boundary conditions are applied to evaluate the primitive variables. At the farfield boundary the flow variables are set to their freestream values for hypersonic inflow conditions whereas for outflow conditions the flow variables are extrapolated by employing the solution of the computational domain.

3 Geometry and Mesh Generation

3.1 Geometry of the TSTO vehicle system

The complete geometry of the TSTO vehicle system consists of two vehicles, namely EOS vehicle as the orbital stage and ELAC vehicle as the carrier stage. A side view and top view of the both stages including all relevant geometric quantities is shown in Fig. 2.

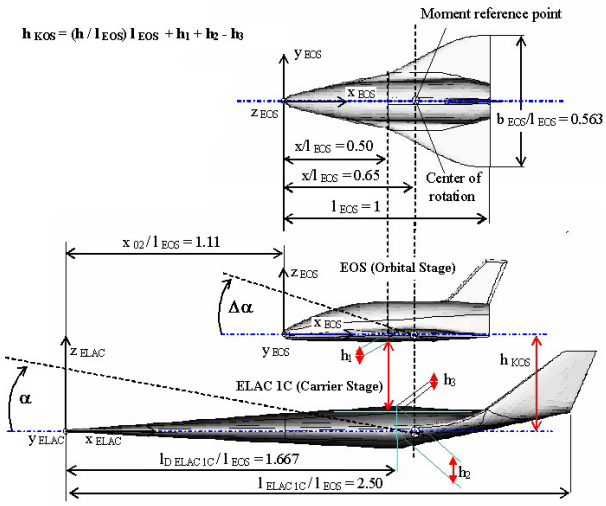

Fig. 2. Geometry of two-stage space transportation system.

The angle of attack (α) is measured based on the X-axis of the ELAC 1C model. The two parameters used in this investigation, namely relative distance (h/l_{EOS}) and relative angle of attack (Δα) are also shown in Fig. 2. The relative angle of attack (Δα) is calculated based on the X-axis of the EOS model.

3.2 Mesh Generation Procedure

In order to obtain structured meshes for the complex space vehicle, a multiblock segmentation of the computational domain of

interest is made using ICEMCFD HEXA by defining the block topology. The refined block topology can be produced by splitting and merging the block, as well as using a special tool called O-grid.

Once the overall blocks are prepared, the points for each block are distributed along the edge of the block. It is necessary to concentrate a major number of points in critical regions such as on leading- and trailing-edge sections of the main wing and the vertical tail of the EOS and the wing tip of the ELAC 1C, and in the wake region behind the base of both vehicles. The point distribution becomes also denser when the points approaching the body surface. The internal points on the face and in the volume of each block are generated by interpolating the given points. The initial computational mesh is shown in Fig. 3. The computational domain is divided into 45 blocks arranged in a hybrid C-O topology. The overall mesh consists of more than 1.1 million volumes and 1.3 million nodes.

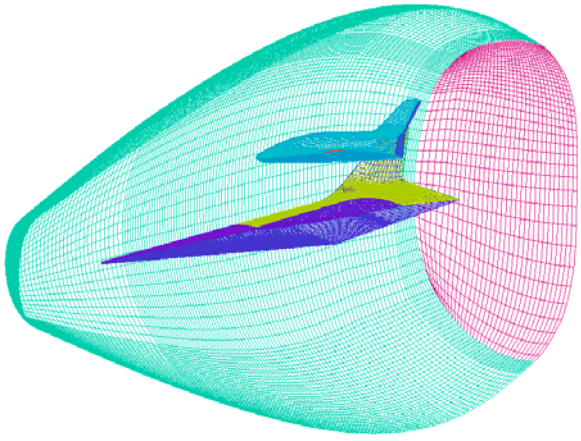

Fig. 3 The initial mesh of the space vehicle

The second step of mesh generation is intended to improve the smoothness as well as the orthogonality of the grids. The initial grid is smoothed using the solution of a system of Poisson vector equation [17]

$$g^{11}(\mathbf{r}_{\xi\xi}+\mathbf{P}\,\mathbf{r}_{\xi})+g^{22}(\mathbf{r}_{\eta\eta}+\mathbf{Q}\,\mathbf{r}_{\eta})+ \qquad (8)$$

$$g^{33}(\mathbf{r}_{\varsigma\varsigma}+\mathbf{R}\,\mathbf{r}_{\varsigma})=\mathbf{0}$$

with $\mathbf{r}=[x,y,z]^T$, ξ,η,ς curvilinear coordinates, and g^{ij} as the covariant metric coefficients with superscripts i,j =1,2,3. The source terms **P**, **Q**, **R** are responsible for the motion of the grid lines and provide the control of grid point spacing and distribution. The result of smoothed grids is given shown in Fig. 4.

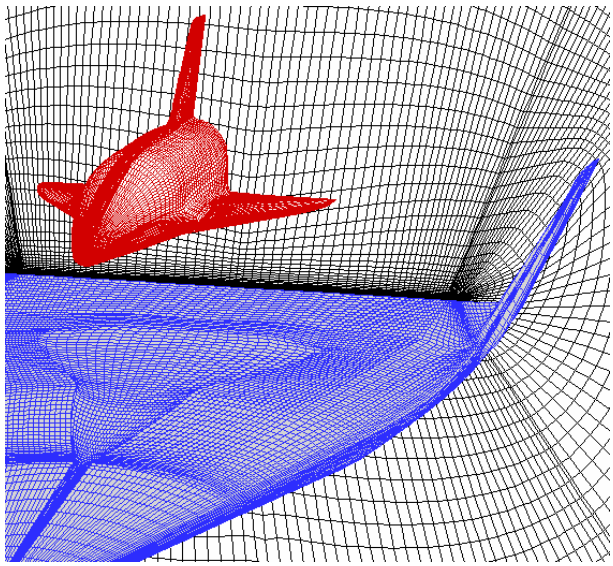

Fig. 4. Smoothed mesh of the space vehicle

In order to provide the solution of unsteady flow due to the moving solid surface of the orbital stage EOS during the separation manoeuvre, a dynamic mesh must be generated for each time step according to the prescribed motion. Because of the motion-induced mesh deformation near the body of the orbital stage, it is necessary to smooth the mesh again using the Poisson algorithm. The mesh motion is limited in given regions around the EOS model that was generated with the O-grid topology. The inner boundary of the mesh at which the solid surface resides has to conform to the motion of the EOS surface at all times. The mesh outer boundary of the O-grid is free to move or is fixed. The velocity of the mesh as well as the deformation of the cells is considered in the unsteady transformation of the Euler equations.

The orbital stage performs harmonically motions simultaneously in relative angle of attack and distance, each of them described as follows:

$$\alpha(\tau) = \alpha_0 + \frac{(\alpha_1 - \alpha_0)}{2}\left(1 - \cos(k\tau)\right)$$
$$h(\tau) = h_0 + \frac{(h_1 - h_0)}{2}\left(1 - \cos(k\tau)\right) \quad (9)$$

where τ is time step and k is reduced frequency. The α_0, h_0, α_1 and h_1 are the relative angle of attack and distance at the initial position and the end position of the separation process, respectively. The pitching reference point is x/L_{EOS} = 0.65 with respect to the nose of the EOS stage.

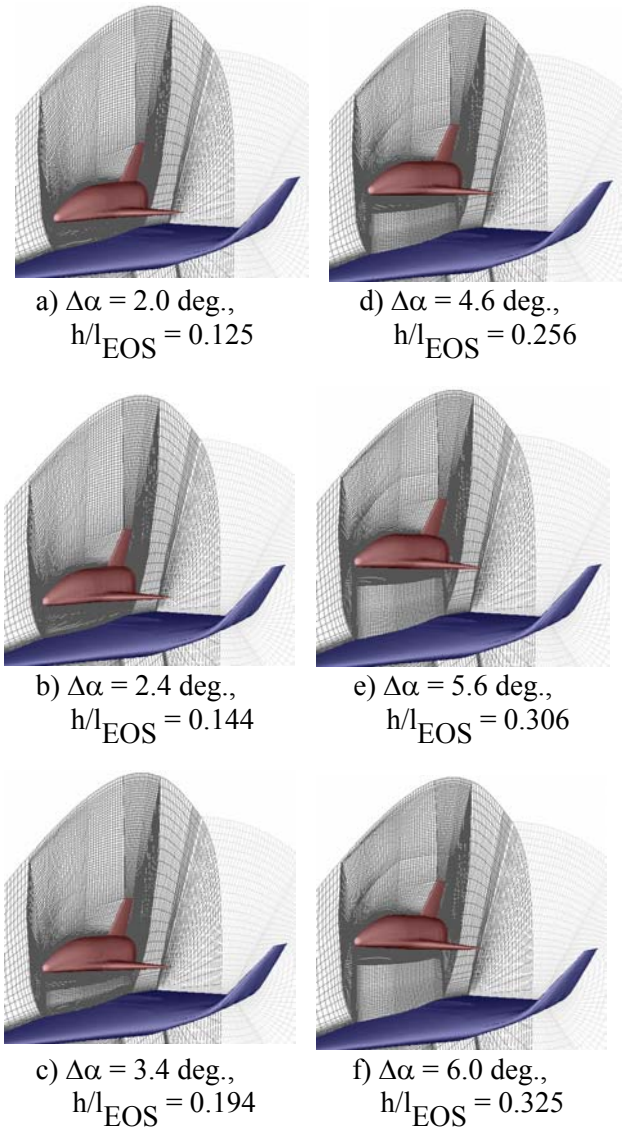

a) Δα = 2.0 deg., h/l_{EOS} = 0.125
d) Δα = 4.6 deg., h/l_{EOS} = 0.256
b) Δα = 2.4 deg., h/l_{EOS} = 0.144
e) Δα = 5.6 deg., h/l_{EOS} = 0.306
c) Δα = 3.4 deg., h/l_{EOS} = 0.194
f) Δα = 6.0 deg., h/l_{EOS} = 0.325

Fig. 7. Dynamic mesh of the space vehicle.

The dynamic mesh for the unsteady simulation of the separation manouevre is performed with the initial position of the orbital stage (α_0 = 2.0 deg.; h_0 = 0.125) and the end position (α_1 = 6.0 deg.; h_1 = 0.325). From the lower to the upper position, 20 time steps (half cycle) are applied on the cosine function in equations (9) with the reduced frequency of 1.0. Fig. 5 shows the results of six different amplitudes of the dynamic grid.

4 Analysis of the Computational Results

4.1 Comparison between Computational and Experimental results

The validation of the computation is performed by comparing the outputs such as flow behaviours and aerodynamic characteristics to the coresponding experimental data. The experimental data were produced using the T-313 tunnel of ITAM (Institute of Theoretical and Applied Mechanics, Russian Academy of Sciences, Siberian Branch), Novosibirsk [18].

Fig. 8 (a) and (b) show a schlieren picture and relative density contours for Ma = 4.04, α = 0.0 deg., Δα = 0.0 deg. and h/l_{EOS} = 0.225. The density contours are obtained at the symmetry plane. The relative density is stated as a ratio value of the density at a certain point of the flowfield to freestream density, ρ/ρ_∞. Qualitatively, almost all flow features of the experimental result shown in Fig. 8 (a) can be captured in the simulation with satisfactory accuracy as shown in Fig. 8 (b). At this condition, the bow shock wave of ELAC 1C impinges on the bow shock of EOS closed to the EOS nose. The bow shock wave of EOS spreads out downstream, but in the symmetry plane it can only be seen above and below of the EOS surface. A part of the bow shock wave goes to the flowfield above of EOS forming a line with a certain angle, φ_u, the other part goes to the flowfield beneath the EOS forming another line with a certain angle, φ_l. The differences of the

bow shock angle between computational and experimental results are in the order of ± 0.5 deg. Subsequently, the latter shock wave hits the middle part of the ELAC 1C surface. While flow on the upper surface of ELAC 1C experiences an expansion through a beginning of the curvature of the ELAC 1C cavity, it forms expansion waves in the flow region between ELAC 1C and EOS stages, but this phenomena can not be shown clearly in the simulation.

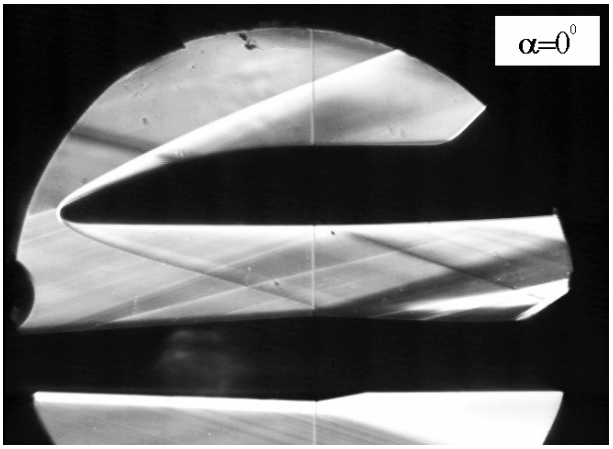

(a) Schlieren picture

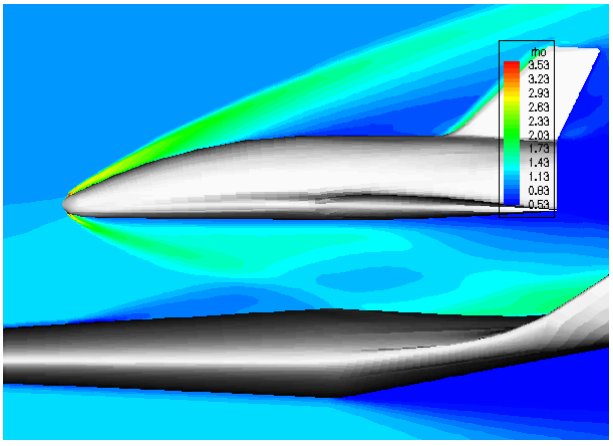

(b) Relative density contours

Fig. 8. Comparison between computational and experimental results: Ma = 4.04, α = 0.0 deg., Δα = 0.0 deg., h/l_{EOS} = 0.225.

At the cavity the flow also exhibits a shockwave due to the curved surface downstream. This shock wave also spread out in the same region. Both the expansion and shock waves interact with the extended bow shock of EOS occurring in the middle flow region between ELAC 1C and EOS stages. The shock wave continues through the flow field and hits the rear part of the lower surface of EOS. At the lower surface of ELAC 1C, the expansion wave can be simulated well.

Concerning the aerodynamic characteristics including lift coefficient (C_L), drag coefficient (C_D) and pitch moment coefficient (C_m), tables 1 and 2 give the computational and experimental results for the orbital stage (EOS) and carrier stage (ELAC 1C), respectively.

	C_L	C_D	C_m
Computation	0.0292	0.0293	-0.0073
Experiment	0.0366	0.0337	-0.0072

Table 1. Aerodynamic characteristics of the Orbital Stage (EOS)

	C_L	C_D	C_m
Computation	-0.0504	0.0133	0.0077
Experiment	-0.0491	0.0164	0.0089

Table 2. Aerodynamic characteristics of the Carrier Stage (ELAC 1C)

Comparing the computational result to the experimental results in tables 1 and 2, the calculated aerodynamic characteristics for the carrier stage give more satisfactory agreement to the experiment results than that of the orbital stage. This is caused by the complex aerodynamic interactions due to shock waves and expansion waves occuring on a larger part of the orbital stage area compared to the carrier stage. At the same time it is indicated as mentioned before that the prediction of the bow shock wave angles occurs on the orbital stage with the error of ± 0.5 deg.

4.2 The influences of the 'separation' parameters

As mentioned above, the effects of relative incidence and relative distance are investigated. Related to the relative angle of attack change, during the setup of the test model in the wind tunnel test section, the EOS stage rotates around the moment reference point located at 0.65 of the fuselage length of the EOS from the EOS nose. At the same time the ELAC stage is in a rest. For the relative distance change, the EOS stage translates vertically from the ELAC 1C stage.

Tables 3 and 4 provides the aerodynamic charcteristics at various relative angles of attack for the orbital stage and carrier stage, respectively. For the orbital stage, the increased relative angle of attack provides the increment of lift coefficient that is equivalent to the amount of the relative angle of attack. But, this affects the decreased lift coefficient of the ELAC 1C in a limited value, see Table 4. Concerning the comparison of the computational and the experimental results, the differences of the lift coefficient increases with the increase in relative angle of attack, while for the ELAC 1C stage the calculated lift coefficient provides a good agreement with the experimental data.

The calculated drag coefficient for the EOS stage increases with the increase in relative angle of attack, but the measured drag coefficient decreases. This is due to the calculated drag coefficient is very sensitive to the location of interaction between the upper ELAC bow shock wave and the EOS bow shock wave. When the upper ELAC bow shock wave hits the EOS bow shock wave just in the front of the EOS nose, the calculated drag coefficient provides a good agreement with the experimental data. But when the upper ELAC bow shock strikes on the upper EOS bow shock wave the calculated drag coefficient presents an under estimation, and contrarily, when it hits the lower EOS bow shock wave the computed drag coefficient shows an over estimation. In addition, for the ELAC 1C stage, there is no significant change in the drag coefficient with increasing the relative angle of attack.

Computation	C_L	C_D	C_m
$\Delta\alpha = 0$ deg.	0.0292	0.0293	-0.0073
$\Delta\alpha = 2$ deg.	0.0626	0.0322	-0.0147
$\Delta\alpha = 5$ deg.	0.1104	0.0368	-0.0259
Experiment	C_L	C_D	C_m
$\Delta\alpha = 0$ deg.	0.0366	0.0337	-0.0072
$\Delta\alpha = 2$ deg.	0.0747	0.0326	-0.0069
$\Delta\alpha = 5$ deg.	0.1311	0.0304	-0.0082

Table 3. Aerodynamic characteristics of the Orbital Stage (EOS) at various relative angles of attack at Ma = 4.04, $\alpha = 0.0$ deg., $h/l_{EOS} = 0.225$.

Computation	C_L	C_D	C_m
$\Delta\alpha = 0$ deg.	-0.0504	0.0133	0.0077
$\Delta\alpha = 2$ deg.	-0.0556	0.0131	0.0086
$\Delta\alpha = 5$ deg.	-0.0628	0.0131	0.0105
Experiment	C_L	C_D	C_m
$\Delta\alpha = 0$ deg.	-0.0491	0.0164	0.0089
$\Delta\alpha = 2$ deg.	-0.0538	0.0164	0.0086
$\Delta\alpha = 5$ deg.	-0.0623	0.0163	0.0105

Table 4. Aerodynamic characteristics of the Carrier Stage (ELAC 1C) at various relative angles of attack at Ma = 4.04, $\alpha = 0.0$ deg., $h/l_{EOS} = 0.225$.

For all relative angles of attack ($\Delta\alpha$), the orbital stage (EOS) provides a negative pitching moment coefficient, while the carrier stage (ELAC 1C) presents positive pitching moment. This means that with increasing $\Delta\alpha$ the nose down magnitude of the EOS will increase which has to be carefully addressed in the flight

control system. In addition, the predictions of the pitching moment coefficient for the ELAC 1C stage give a good agreement with the experimental data for all the relative angles of attack, but for the EOS model the prediction only produce a good agreement with the experimental data when the relative angle of attack is 0.0 deg.

Concerning the effects of the relative distance, tables 5 and 6 provide the calculated and measured aerodynamic characteristics at relative distances of 0.225 and 0.325 for the orbital stage and carrier stage, respectively.

For all aerodynamic characteristics the comparison between the computational and experimental results show a good consistence. Increasing relative distance gives a decrease in lift coefficient for the EOS stage, but a less negative lift coefficient for the ELAC 1C stage. The drag coefficient for the EOS and ELAC 1C stages decrease with increasing relative distance. For all relative distances (h/l_{EOS}), the EOS stage provides a negative pitching moment coefficient, while the ELAC 1C stage presents a positive pitching moment. With increasing relative distance the pitching moment coefficient for the EOS model becomes more negative. This has to be considered as it may have an impact on the stability of the vehicle during separation.

Computation	C_L	C_D	C_m
$h/l_{EOS} = 0.225$	0.0292	0.0293	-0.0073
$h/l_{EOS} = 0.325$	0.0225	0.0287	-0.0161
Experiment	C_L	C_D	C_m
$h/l_{EOS} = 0.225$	0.0366	0.0337	-0.0072
$h/l_{EOS} = 0.325$	0.0332	0.0317	-0.0137

Table 5. Aerodynamic characteristics of the Orbital Stage (EOS) at various relative distances at Ma = 4.04, α = 0.0 deg., $\Delta\alpha$ = 0.0 deg.

Computation	C_L	C_D	C_m
$h/l_{EOS} = 0.225$	-0.0504	0.0133	0.0077
$h/l_{EOS} = 0.325$	-0.0439	0.0130	0.0057
Experiment	C_L	C_D	C_m
$h/l_{EOS} = 0.225$	-0.0491	0.0164	0.0089
$h/l_{EOS} = 0.325$	-0.0394	0.0164	0.0062

Table 6. Aerodynamic characteristics of the Carrier Stage (ELAC 1C) at various relative distances at Ma = 4.04, α = 0.0 deg., $\Delta\alpha$ = 0.0 deg.

4.3 Unsteady Flow Simulation Results

The calculations of unsteady separation are performed after the steady state solution is obtained. The steady state solution is calculated based on the initial state of M_∞ = 4.04, α = 0.0 deg., $\Delta\alpha$ = 2.0 deg. and h/L_{EOS} = 0.125. Using the steady state results, the unsteady simulations of the separation manouvre of the orbital stage are then computed for each time step according to a pitching motion until the residual reaches the convergence criteria of about 5 x 10^{-4} in change of relative density. In order to obtain a proper solution the simulations are previously run 360 degrees (one cycle) consisting of 40 time steps from the initial position and back to the initial position again. The simulations are performed for a reduced frequency of k = 1.0. The results of six different pictures of instantaneous contours of relative density on the symmetry plane are shown in Fig. 9.

It is indicated that the bow shock wave of ELAC 1C impinges on the bow shock of EOS closed to the EOS nose. The bow shock wave of ELAC moves from the upper bow shock wave part to the lower bow shock wave part of EOS corresponding to the motion of EOS. Before affecting the EOS bow shock, the line of the ELAC 1C bow shock becomes bending due to the induced vertical velocity flow. This does not occur in the steady flow simulation.

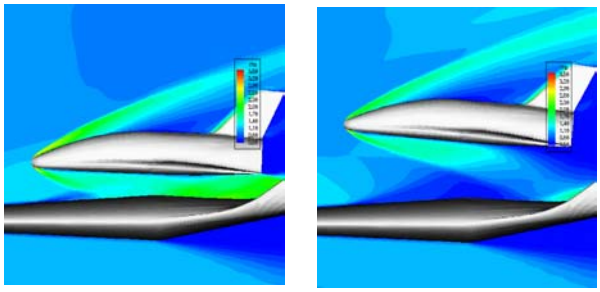

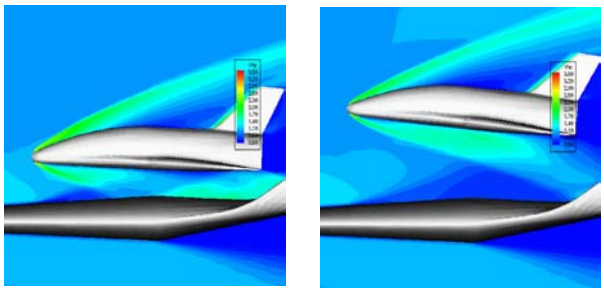

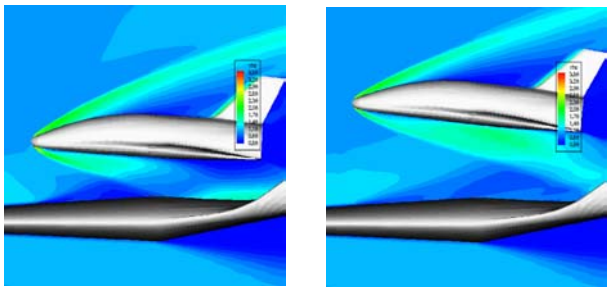

Fig. 9. Instantaneous density contours at six different time levels during separation. Ma_∞ = 4.04, α = 0.0 deg., Δα =2.0-6.0 deg., h/l_{EOS} = 0.125-0.325, k = 1.0.

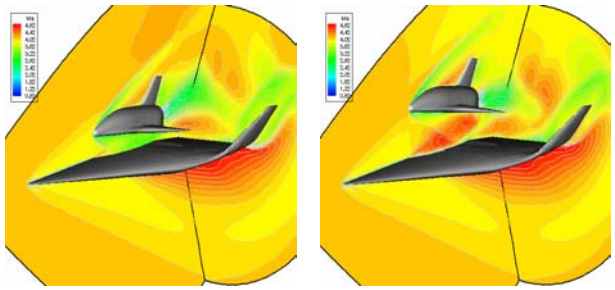

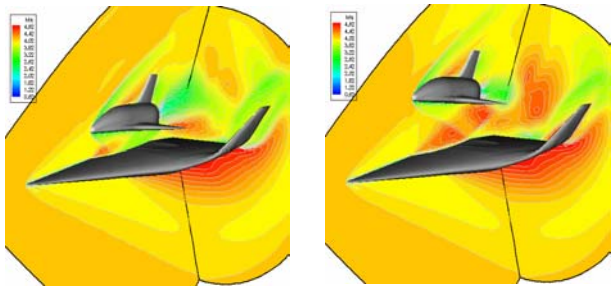

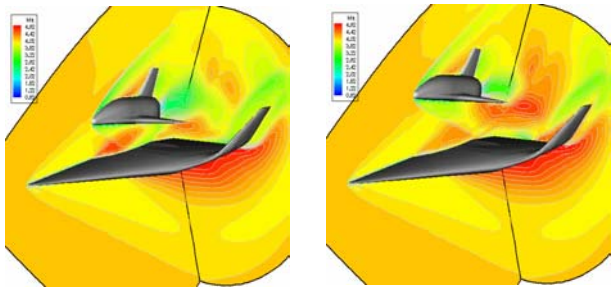

Fig.10. Instantaneous Mach number contours at six different time levels during separation Ma_∞ = 4.04, α = 0.0 deg., Δα =2.0-6.0 deg., h/l_{EOS} = 0.125-0.325, k = 1.0.

Subsequently, the bow shock wave of EOS spreads out downstream, but in the symmetry plane this effect can only be seen above and below of the EOS surface, Fig. 9. The upper bow shock angle seems to increase when it is closer to the maximum amplitude. In the gap region between the EOS and ELAC 1C stages, complex aerodynamic interactions including shock waves, expansion waves and reflected shock waves occur. With increasing amplitudes of the EOS stage the location of the interaction points of the bow shock waves, expansion waves and reflected shock waves move further downstream.

Fig. 10 depicts the unsteady Mach number contours in 3D views. With increasing amplitude higher Mach numbers are shown in the gap region and in the region below the rear part of ELAC 1C. The suction flow occurs in this region just on the upper surface of EOS. The change of Mach number distribution along the surfaces of the EOS and ELAC 1C vehicles will provide a change of aerodynamic loads during the separation process.

Concerning the aerodynamic characteristics with respect to the unsteady motion of the space transportation system, Fig. 11 shows the graphs

of the lift, drag and pitch moment coefficients versus amplitudes of relative angle of attack and relative distance.

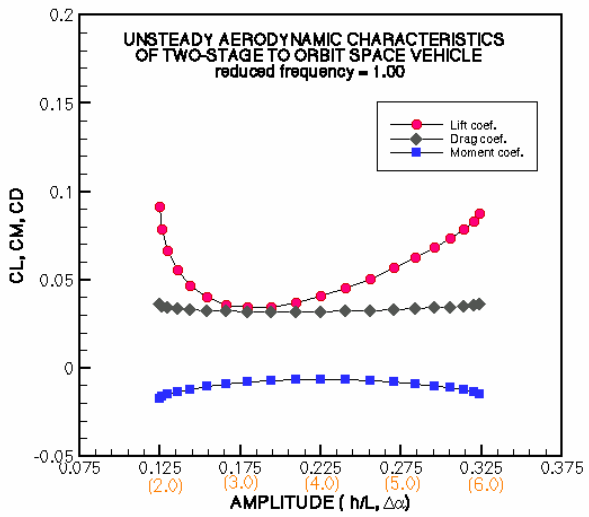

Fig. 11. Unsteady aerodynamic characteristics of the space transportation system at Ma_∞= 4.04, α = 0.0 deg., Δα =2.0-6.0 deg., h/l_{EOS} = 0.125-0.325, k = 1.0.

Starting from the lower amplitude, namely the relative angle of attack of 2.0 deg. and relative distance of 0.125, the lift coefficient decreases with increasing amplitude and then before reaching the middle position the lift coefficient increases with a further increase in the amplitude. The drag coefficient slightly decreases with increasing amplitude and then the drag coefficient increases at higher amplitudes. While, in the beginning of the separation, the pitching moment coefficient becomes less negative, the pitching moment coefficient becomes more negative with increasing amplitude. The change of lift and pitching moment coeffient during the separation must be carefully considered as it has an impact on the EOS vehicle stability.

4 Conclusions and Outlook

Steady numerical simulations for the flow field of a Two-Stage-To-Orbit space transportation system have been accomplished with good to excellent agreement to the experimental values at various relative angles of attack and relative distances.

Substantiated by the unsteady aerodynamic characteristics, unsteadiness must be carefully considered in the beginning of the separation manoeuvre when the orbital stage lift decreases. In addition, the drag coefficient of the orbital stage slightly decreases with increasing the relative distance from the carrier stage. The pitching moment coefficient shows a decrease followed by an increase of nose down magnitude with increasing distance and relative angle of attack which has to be carefully addressed in the flight control system.

For future research, a further investigation of the separation process of the space transportation system with considering a supporting mechanism to elevate the orbital stage from a position closer to the carrier stage to a position of a full stand of the mechanism is proposed. It is intended to initially shift the orbital stage to a position, that the separation process progresses safely and efficiently.

Acknowledgement

The subject of this paper is part of the research undertaken in the Collaborative Research Center 255 “Transatmospheric Flight Systems – Fundamentals of Aerothermodynamics, Propulsions and Flight Mechanics” of the German Research Association (Deutsche Forschungsgemeinschaft, DFG) at the Technische Universität München.

References

[1] Russo, G. Next generation space transportation system. *Aerotecnica Missili e Spazio*, Vol. 81, Feb. 2002.

[2] Hirschel, E.H. The technology development and verification concept of the German hypersonic programme. Aerothermodynamics and propulsion integration for hypersonic vehicles. *AGARD-R-813*, pp 12-1-12-15, 1996.

[3] Laschka, B., and Breitsamter, C. Transatmosphärische Flugsysteme–Grundlagen der Aerothermodynamik, Antriebe und Flugmechanik. *Sonderforschungsbereich 255*, June 2001.

[4] Decker, J.P., and Gera, J. An exploratory study of parallel stage separation of reusable launch vehicles. *NASA TN D-4765*, Oct. 1968.

[5] Bernot, P.T. Abort separation study of a shuttle orbiter and external tank at hypersonic speed. *NASA TM X-3212*, May 1975.

[6] Bonnefond, T., Kharitonov, A.M., Brodetsky, M.D., Vasenyov, L.G., Adamov, N.P., and Derunov, E.K. Separation of winged vehicles in supersonic. *AIAA-95-6092, 6th International Aerospace Planes and Hypersonic Technologies conference*, 3-7 April 1995.

[7] Bonnefond, T., Adamov, N.P., Brodetsky, M.D., Vasenyov, L.G., Derunov, E.K., and Kharitonov, A.M. An experimental investigation of aerodynamic interference of TSTO winged during separation. *J. Thermophysics and Aeromechanics*, Vol.3, No. 3 and No. 4, 1996.

[8] Weiland, C. Stage separation aerodynamics. Aerothermodynamics and propulsion integration for hypersonic vehicles. *AGARD-R-813*, pp 11.1-27, 1996.

[9] Rochholz, H. Huber, T., and Matyas, F. Unsteady airloads during separation of an idealized two-stage hypersonic vehicle. *Zeitchrift für Flugwissenschaften und Weltraumforchung*, Band 19, Heft 1, pp.2-9, 1995.

[10] Cvrlje, T., Breitsamter, C., and Laschka, B. Unsteady and coupling aerodynamic effects on the lateral motion in hypersonic flight. *AIAA-99-4832, 9th International Space Planes and Hypersonic Systems and Technologies conference*, 1-5 Nov. 1999.

[11] Cvrlje, T., Breitsamter, C., Weishäupl, C., and Laschka, B. Euler and Navier-Stokes simulations of two-stage hypersonic vehicle longitudinal motions. *J. of Spacecraft and Rockets*, Vol. 37, No.2, March-April 2000.

[12] Brenner, P. Numerical simulation of three dimensional and unsteady aerodynamics about bodies in relative motion applied to a TSTO separation. *5th AIAA International Aerospace Planes and Hypersonic Technology Conference*, AIAA-93-5142, 1993.

[13] Schröder, W., Behr, R., and Menne, S. Analysis of hypersonic flows around space transportation system via cfd methods. *AIAA-93-5067*, 1993.

[14] Decker, K. Aerodynamik eines zweistufigen Raumtransportsystems beim Wiedereintritt und während der Separation. *Dissertation*, Technische Universität München, Dec. 2003.

[15] Radespiel R., and Kroll N. Accurate flux vector splitting for shock and shear layers. *Journal of Computational Physics*, Vol. 121, pp. 66-78, 1995.

[16] Liou, M. S., and Steffen, Ch. A new flux splitting scheme. *Journal of Computational Physics*, Vol. 107, pp. 23-39, 1993.

[17] Thompson, J. F., Soni, B. K., and Weatherill, N.P. *Handbook of grid generation*, CRC Press LLC, 1999.

[18] Kharitonov, A., Brodetsky, M., Vasenyov, L., Adamov, L., Breitsamter, C., and Heller, M. Investigation of aerodynamic characteristics of the models of a two-stage aerospace system during separation. *Final Report*, Institute of Theoretical and Applied Mechanics, Russian Academy of Sciences, Siberian Division, Novosibirsk, Russia, and Lehrstuhl für Fluidmechnik and Lehrstuhl für Flugmechnik und Flugreglung, Technische Universität München, Nov. 2000.